Thermal conductivity profile in the Nankai accretionary prism at IODP NanTroSEIZE Site C0002: estimations from high-pressure experiments using input site sediments

Weiren Lin[1*], Takehiro Hirose[2], Osamu Tadai[3], Wataru Tanikawa[2], Kazuya Ishitsuka[1], Xiaoqiu Yang[4, 5]

[1]*Graduate School of Engineering, Kyoto University, Kyoto 615-8540, Japan*

[2] *Kochi Institute for Core Sample research, Japan Agency for Marine-Earth Science and Technology, Nankoku, Japan*

[3] *Marin Works Japan LTD, Nankoku, Japan*

[4] *CAS Key Laboratory of Ocean and Marginal Sea Geology, South China Sea Institute of Oceanology, Guangzhou 510301, China*

[5] *Southern Marine Science and Engineering Guangdong Laboratory (Guangzhou), Guangzhou 511458, China*

*Corresponding author.

C1-1-109, Kyotodaigaku-Katsura, Nishikyo-Ku, Kyoto 615-8540, Japan

E-mail: lin@kumst.kyoto-u.ac.jp

Abstract

Depth profiles of sediment thermal conductivity are required for understanding the thermal structure in active seismogenic zones. During the Nankai Trough Seismogenic Zone Experiment (NanTroSEIZE), a scientific drilling project of the International Ocean Discovery Program, a borehole penetrated to a depth of 3262.5 meters below seafloor (mbsf) at site C0002. Because core samples obtained from below ~1100 mbsf in an accretionary prism are limited, a thermal conductivity profile over such depths usually determined by laboratory measurements using core samples is not available. To obtain the thermal conductivity profile at site C0002, we used core samples collected from sediments that overlay the in-coming subducting oceanic basement at NanTroSEIZE site C0012, which can be considered to have the same mineral composition as the accretional prism at site C0002. The thermal conductivity of the C0012 core samples was measured at high pressure to simulate subduction by reducing the sample porosity. We measured the thermal conductivity of six core samples from 144–518 mbsf at site C0012 up to a maximum effective pressure of ~50 MPa, corresponding to depths greater than ~4 kmbsf. We obtained an empirical relation between thermal conductivity λ_{Bulk} and fractional porosity ϕ for the Nankai Trough accretionary prism as $\lambda_{Bulk} = \exp(-1.09\,\phi + 0.977)$. Based on porosity data measured using core/cuttings samples and data derived from P-wave velocity logs, we estimate two consistent and complete thermal conductivity profiles down to ~3 kmbsf in the Nankai Trough accretionary prism. These profiles are consistent with the existing thermal conductivity data measured using limited core samples.

Plain Language Summary:

Depth profiles of sediment thermal conductivity are required for understanding the thermal structure and earthquake occurrences in active seismogenic zones such as the Nankai Trough, SW Japan. The depth profile in Nankai Trough accretionary prism, however, is not available because sediment drill core samples from great depths are hard to be obtained. We collected six core samples from shallower sediments that overlay the in-coming subducting oceanic basement at Nankai Trough drill site C0012 by IODP, which can be considered to have the same solid grain components as the accretional prism at site C0002. The thermal conductivity of the C0012 core samples was measured at high pressure. We pressurized the core samples to simulate deeper sediments in accretionary prism by reducing sample porosity. As the result, we obtained an empirical relation between thermal conductivity and porosity for the Nankai Trough sediments, then estimated thermal conductivity profiles down to ~3 km below seafloor based on porosity profiles in the Nankai Trough accretionary prism.

Key Points:

- Two consistent thermal conductivity profiles were obtained down to ~3 km below the seafloor in the Nankai Trough accretionary prism.
- We pressurized shallow overlying sediments on an oceanic plate to simulate deeper sediments in an accretionary prism by reducing porosity.
- We obtained an empirical thermal conductivity–porosity relation for Nankai Trough sediments applicable to a basin and accretionary prism.

Keywords: Thermal conductivity, Porosity, Sediments, High pressure experiments, Nankai Trough, Accretionary Prism

1. Introduction

The Nankai convergent subduction zone in southwest Japan is one of the most active seismogenic zones in the world, where megathrust earthquakes (Mw > 8) have occurred over recurrence intervals of 100–200 years (Ando, 1975), which are comparatively shorter than other main seismogenic subduction zones. For a comprehensive understanding of this seismogenic zone, the International Ocean Discovery Program (IODP, known as the Integrated Ocean Drilling Program before 2013) conducted 13 expeditions as part of the Nankai Trough Seismogenic Zone Experiment (NanTroSEIZE) project from 2007 to 2019 (Kinoshita et al., 2006, Tobin et al., 2019a). The NanTroSEIZE is a multidisciplinary investigation of fault mechanics and seismogenesis along subduction megathrusts and includes reflection and refraction seismic imaging, direct sampling by drilling, in-situ measurements, and long-term monitoring in conjunction with laboratory and numerical modeling studies (Tobin et al., 2019b).

Temperature plays a key role in seismogenesis at subduction zones and is thought to govern the nature of slip along active subduction thrusts, as well as the upper and lower transitions of seismogenic zones (e.g., Wang et al., 1995; Harris and Wang, 2002; Yamano et al., 2003). Specifically, temperature controls the rupturing properties of fault materials (e.g., slip velocity dependence of the frictional coefficient), pore fluid transportation properties that affect pore fluid pressure and thus fault strength, and water-rock reactions that affect fault strength recovery (e.g., Stesky et al., 1974; Scholz, 1998; Tanikawa et al., 2013; Mizutani et al., 2017). Conversely, thermal conductivity also controls the coseismic temperature that increases in and around fault slip zones caused by frictional heating, and affects the postseismic diffusion process of frictional heating and temperature recovery processes (e.g., Fulton et al., 2013).

Depth profiles of the thermal conductivity of sediments in accretionary prisms in subduction zones are necessary and important for understanding the temperature structure and heat flow around a megathrust (Harris et al., 2011; Spinelli, 2014; Tanikawa et al., 2016). At the centerpiece site C0002 of the NanTroSEIZE, a borehole was penetrated to a depth of 3262.5 meters below seafloor (mbsf), which is the deepest of all of the scientific ocean drilling programs (Tobin et al., 2019a). However, a very limited number of core samples were collected below ~1100 mbsf at site C0002, which is located in the accretionary prism above the seismogenic zone. Consequently, available thermal conductivity data remain limited in the accretionary prism because thermal conductivity measurements require core samples. Fortunately, a complete porosity depth profile is available from laboratory measurements using continuously recovered cuttings samples. A porosity depth profile can also be derived from P-wave velocities and/or resistivity logs. The problem is therefore how to reasonably establish the relationship between the thermal conductivity and porosity of the sediments in the accretionary prism of site C0002.

IODP expeditions 322 and 333 of the NanTroSEIZE project drilled at input sites C0011 and C0012, which are on the Philippine Sea plate and will eventually be subducted beneath the Eurasian plate (Figures 1 and 2; Underwood et al., 2010; Expedition 333 Scientists, 2012a). The overlaying sediments at the input site will be transported to the underthrust strata and/or accrete to the accretionary prism above the plate boundary fault (décollement; Figure 2). The sediment core samples recovered at an input site therefore allow estimation of the thermal conductivity of the accretionary prism because sediments from both the input site and accretionary prism are expected to have the same or similar solid grain components. Expedition reports used X-ray diffraction (XRD) analysis to confirm that the major mineral composition of sediments (clay minerals, quartz, feldspar, calcite) is the same at input site C0012 as the accretionary prism down to 3058.5 mbsf at

site C0002 (Expedition 322 Scientists, 2010; Expedition 333 Scientists, 2012b; Tobin et al., 2015b). The thermal conductivity of the sediments will also change during subduction because compaction will decrease their porosity with depth. The relationship between thermal conductivity changes and porosity reductions caused by increased pressure should therefore be simulated in laboratory measurements using core samples from shallow input sites. This relationship allows estimations of thermal conductivity of the deeper accretionary prism once the porosity is obtained.

Many previous studies have measured the thermal conductivity of hard rocks at high pressure, even up to pressures above 1 GPa (e.g., Horai and Susaki, 1989; Pribnow et al., 1996; Seipold and Huenges, 1998; Kukkonen et al., 1999; Osako et al., 2004; Xu et al., 2004; Abdulagatova et al., 2009), but only a few measurements from ocean sediments have been reported (e.g., Morin and Silva, 1984; Lin et al., 2011). There is no systematic data set in the literatures of the effect of pressure on the thermal conductivity of subduction zone sediments for simulating subduction. Furthermore, no experimental data have been published on the effects of pressure on the thermal conductivity of sediments from the Nankai Trough region except for our preliminary findings (Lin et al., 2011).

In this study, we measured the thermal conductivity of six core samples from sediments overlaying the subducting Philippine Sea plate under conditions of high confining and pore fluid pressure and monitored the porosity changes of the test samples. The thermal conductivity changes of the sediments were examined over a wide porosity range from ~60% to ~20%, which matches the porosity of the accretionary prism down to ~3 kmbsf (kilometers below the seafloor) and approximately corresponds to the current hole bottom at NanTroSEIZE site C0002. On the basis of this data set, we established an empirical equation that describes the relationship between

thermal conductivity and porosity of the sediments. We then estimated thermal conductivity depth profiles of the accretionary prism above the Nankai seismogenic zone based on the porosity data.

2. Tectonic Setting and Experimental Samples

2.1 Nankai Subduction Zone and NanTroSEIZE

The Nankai Trough region in southwest Japan is one of the most extensively studied subduction zones in the world (e.g., Yamamoto et al., 2013). The subducting Philippine Sea plate is currently moving northwest beneath the Eurasian plate at a rate of ~4–6 cm/yr (Seno et al., 1993; Heki and Miyazaki, 2001; Miyazaki and Heki, 2001), roughly orthogonal to the axis of the Nankai Trough (Figure 1). In this area, Mw 8.0-class earthquakes occur frequently because of the convergence of the Philippine Sea and Eurasian plates. The last two great earthquakes in the Nankai subduction zone occurred in 1944 (Tonankai, M 8.0–8.3) and 1946 (Nankai, M 8.1–8.4), generating tsunamis and causing significant damage in southwestern Japan (Kanamori, 1972). The updip limit of the Nankai Trough seismogenic zone (i.e. locked zone of the plate boundary fault) is up to ~5 kmbsf and considered accessible by the riser drilling vessel *D/V Chikyu*. The NanTroSEIZE project was designed to investigate the mechanics of the subduction megathrust from drilling and a wide range of related studies (Tobin and Kinoshita, 2006; Tobin et al., 2019b). A challenging plan was established to drill through the seismogenic zone to a depth of ~5 kmbsf at site C0002, where the updip limit of the coseismic slip zone of the 1944 Tonankai earthquake is located (Figures 1 and 2). The drilling operations of NanTroSEIZE were performed in multiple expeditions since 2007 as IODP expeditions 314 and 315. A penetration depth of 3262.5 mbsf was achieved in the fourth stage of expedition 358, and will probably be retried in the future (Tobin et

al., 2009a; Tobin et al., 2019b). Conversely, IODP expeditions 322 and 333 were designed to drill on the incoming Philippine Sea plate at two reference sites called “input sites” that included site C0012 and sampled materials including overlaying sediments and basaltic basement (Figures 1 and 2) (Saito et al., 2009). The basement will ultimately subduct into deeper oceanic crust, but the sediments will become the underthrust sediments and/or accrete onto the accretionary prism. They will then compose the seismogenic zone around the plate boundary interface in the future. Site C0012 is located ~31 km seaward of the trench on a basement high (the Kashino knoll) and includes samples of a condensed section from shallow sedimentary rocks to basaltic basement (Underwood et al., 2010; Expedition 333 Scientists, 2012a).

2.2 Core Samples

To estimate the thermal conductivity of the accretionary prism of the Nankai Trough subduction zone (i.e., below the unconformity at ~922 mbsf at site C0002), we collected six sediment core samples that cover all of the lithological units from hole C0012A drilled during expedition 222 in 2009 and C0012D and C0012G during expedition 333 in 2011 at almost the same location (32°44.9′N, 136°55.0′E) (Expedition 222 Scientists, 2010; Expedition 333 Scientists, 2012b). The sediment core samples were taken from a depth range of 144–518 mbsf, and the boundary between overlying sediments and basaltic basement was documented at ~526 mbsf. The water depth at the borehole locations is ~3500 m. The wet bulk density (bulk density of water saturated samples), grain density, porosity, and thermal conductivity of the sediment core samples were measured in the laboratory under atmospheric pressure and room temperature conditions (Table 1). These fundamental physical properties are in good agreement with onboard

measurement results (Expedition 333 Scientists, 2012b). Wet bulk density and porosity were determined using the buoyancy method, in which the sample was dried at ~110 °C (Franklin, 1979).

Multiple boreholes were penetrated at site C0012 during multi expeditions to achieve good quality core samples and completely cover all of the sediments and basaltic basement. From the seafloor to the bottom of the overlaying sediments, the formations are divided into six units. These include units: (I) upper Shikoku basin facies (above ~150 mbsf, hemipelagic deposits, late Miocene to early Pliocene); (II) middle Shikoku basin facies (~150–220 mbsf, hemipelagic deposits, late Miocene); (III) lower Shikoku basin hemipelagic facies (~220–332 mbsf, hemipelagic deposits, middle to late Miocene); (IV) lower Shikoku basin turbidite facies (~332–416 mbsf, hemipelagic deposits and silty turbidity currents, middle Miocene); (V) volcaniclastic-rich facies (~416–528 mbsf in C0012A, hemipelagic deposits, volcaniclastic turbidity currents etc., mainly middle Miocene); and (VI) pelagic clay facies (~500–526 mbsf in C0012G, pelagic deposits including reddish brown calcareous claystone, early Miocene) (Expedition 322 Scientists, 2010 and Expedition 333 Scientists, 2012b). We retrieved one core for each lithological unit mentioned above and the lithology at each depth of the core samples is listed in Table 1. We used the six hemipelagic and pelagic sediment core samples to measure thermal conductivity under high confining and pore fluid pressures and room temperature.

3. Experimental Protocol

In our previous study (Lin et al., 2011), we established a thermal conductivity measurement system for rock samples under high confining pressure but without pore pressure control. The first data set used two soft sediments core samples from site C0001 of NanTroSEIZE and hard rocks

including fresh granites from terrestrial quarries to demonstrate that the measurement methods are effective for examining the effects of high confining pressure on the thermal conductivity of core samples (Lin et al., 2011). For a more exact simulation of not only lithostatic pressure but also pore fluid pressure, we developed a system with a pore pressure control function. This system can monitor pore water drainage and sample deformation under high pressure, and enables the estimation of porosity changes under high-pressure conditions. The apparatus comprises two highly accurate pressure controlling syringe pumps (Teledyne Isco, 260D and 65D) used for controlling the confining and pore pressure and monitoring both pressure and flow volume (Figure 3). This system was first used for thermal conductivity measurements using basaltic samples including a core sample from the same site C0012. For the thermal conductivity measurements, we used the same thermal conductivity meter, QTM-500 (Kyoto Electronics Manufacturing, Kyoto, Japan), as that of Lin et al. (2011), which is based on transient heating of a half-space sample by a line-source (Sass et al., 1984; Galson et al., 1987). We also used the same line-source sensor probe in the high-pressure vessel and data analyses designed and created in the previous study, as well as the same sample assembly as Lin et al. (2011) and Lin et al. (2018) (Figure 4). The rock samples were half cylinders with a ~5-cm diameter and ~10-cm length.

For thermal conductivity measurements using the transient line-source devices of the QTM-500, lower thermal conductivities of the test sample were associated with steeper temperature increases during heating (Lin et al., 2011). In principle, the temperature should increase linearly on a semi-logarithmic scale between temperature and heating time. During our high-pressure measurements, the temperature curves show a nearly linear increasing pattern (Figure 5). The gradient decreases with increasing effective pressure, indicating that the apparent thermal conductivity of the rock and Teflon pair increases with increasing effective pressure.

227 Because the axial direction of the core samples was oriented vertically, the measured
228 thermal conductivity reflects that in the horizontal direction in its in-situ position. Similar to
229 orderly deposited ocean sediments, Lin et al. (2014) showed that the thermal conductivity
230 anisotropy of core samples collected from Japan Trench drilling site C0019 above the plate
231 interface was less than ~3%, which is almost the same as the thermal conductivity precision.
232 To simulate subduction of the overlaying sediments, we increased the confining pressure
233 stepwise to 60 MPa while holding the pore pressure constant at 10 MPa. We then measured the
234 thermal conductivity at each confining pressure. We define the effective pressure P_{eff} as the
235 difference of confining pressure P_c and pore pressure P_p, i.e., $P_{eff} = P_c - P_p$. We set the effective
236 pressures of the thermal conductivity measurements to 1, 5, 10, 20, 30, 40, and 50 MPa (Figure
237 6a). Because all of the sediment core samples used in this study were retrieved from relatively
238 shallow depths (<518 mbsf), effective pressures greater than 5 MPa exceed the maximum pressure
239 the rock of the core sample had experienced. The high pressures thus caused larger deformation,
240 called normal consolidation, and sometimes broke the sealing rubber jacket, after which confining
241 pressure medium (oil) entered the inside of the sample assembly.
242
243 **4. Results**
244
245 **4.1 Thermal Conductivity under High Confining and Pore Pressure Conditions**
246 Figure 6 shows a typical thermal conductivity measurement of core sample C0012A19R1
247 retrieved from ~217 mbsf at site C0012. As a rough estimation from its depth, the maximum
248 effective pressure that the core sample had previously experienced might been ~2 MPa. We loaded
249 the confining pressure to ~1.5 MPa and pore pressure to ~0.5 MPa (effective pressure of ~1.0

MPa) for one day, and then to ~11 and ~10 MPa, respectively, for one day in the second step (Figure 6a). The confining pressure was then increased stepwise to ~12, 15, 20, and 30 MPa but the pore pressure was maintained at ~10 MPa. A few hours after loading to ~30 MPa, the rubber jacket broke and the experiment was terminated after a total of ~43 days.

During the pressure loading and maintenance, water drainage was monitored by a 260D syringe pump used for pore pressure control. The following assumptions were made: a) water intake and output are equal to total pore volume change, and b) the initial porosity of the test sample at the beginning of the experiment is the same as that measured by the buoyancy method using a neighboring sub-sample cut from the thermal conductivity test sample (53.4%, Table 1). The estimated porosity $\phi(t)$ at an arbitrary elapsed time t was determined using:

$$\phi(t) = (V_{WI} - V_{Drain}(t)) / (V_{SI} - V_{Drain}(t)), \quad (1)$$

where V_{SI} is the initial sample volume, V_{WI} is the initial pore volume of the sample saturated by water, $V_{Drain}(t)$ is the volume of water drained at an arbitrary time assumed to be equal to the change of pore volume relative to the initial volume. The pore volume at a given time was calculated by subtracting $V_{Drain}(t)$ measured by the 260D pump from V_{WI}. The sample volume at a given time was calculated by subtracting its volumetric change assumed to be equal to the pore volume change as $V_{SI} - V_{Drain}(t)$. Because the sample assembly and steel tubes for pore fluids in the pressure vessel were deformed during the confining pressure change, we calibrated the system deformation and corrected the raw pump data of water drainage to obtain $V_{Drain}(t)$ for estimating porosity changes in the same way as described in Lin et al. (2018).

The estimated porosity of sample C0012A19R1 is shown in Figure 6b as a function of elapsed time. During the first loading step, the porosity of the core sample decreased by ~2%, possibly caused by a porosity increase owing to rebound accompanied with the in-situ stress relief

by drilling. This decrease may also have some uncertainty owing to air in the sample assembly and experimental system prior to pressurizing. At effective pressure conditions of ~2 MPa or lower, the estimated porosity does not substantially decrease because the sample had already undergone such pressures prior to retrieval from its in-situ depth. However, once the effective pressure conditions (5 and/or 10 MPa) exceed a certain level (~2 MPa) that the sample had previously experienced, its porosity gradually and then significantly decreases. Moreover, the porosity reduction process (consolidation) continues over a long time duration. For example, the porosity decrease did not completely stabilize even ~30 days after pressurization to 20 MPa confining pressure. As a result, the porosity of this sample loaded to an effective pressure 10 MPa decreased by ~15% over ~43 days.

The thermal conductivity was measured multiple times at each pressure condition ("+" symbols in Figure 6a represent measuring points) in cases that the pressure condition was held for more than one day, amounting to an average of one measurement per day on weekdays. Thermal conductivity measurements were repeated six or seven times at each measuring point. The measured values show a small degree of scatter with a relative standard deviation of <3%, as shown in Figure 6c where measured values and their mean are represented by blue squares and red circles, respectively. The full thermal conductivity data set measured from the six sediment core samples is provided in the supplemental information.

The results of sample C0012A19R1 show that thermal conductivity increases not only with effective pressure but also over elapsed time or when porosity decreases even under the same effective pressure condition (Figures 6b and 6c). We also measured thermal conductivity after termination of the experiment on the 42nd day and one more time on the 43rd day under atmospheric pressure conditions. Surprisingly, the results show a lower thermal conductivity on

296 the 43rd day than the 42nd day (Figure 6c). This may reflect time-dependent strain recovery caused
297 by the pressure relief. Byrne et al. (2009), Yamamoto et al. (2013), and Oohashi et al. (2017)
298 successfully applied this strain-recovery principle to constrain the three-dimensional in-situ stress
299 state of the NanTroSEIZE project.
300
301 **4.2 Thermal Conductivity Changes with Increasing Pressure and Decreasing Porosity**
302 Figure 7 shows thermal conductivity values measured at various effective pressure
303 conditions for all the six sediment samples in this study and the basalt sample after Lin et al. (2018).
304 Thermal conductivity was also measured under atmospheric pressure conditions prior to increasing
305 the confining and pore pressure. The results show that thermal conductivity generally increases
306 with depth (Table 1) but appears to depend on the sample lithology and detailed mineral
307 composition. Overall, the thermal conductivity of wet core samples (sea water saturated) increases
308 with increasing effective pressure (Figure 7). As mentioned, as the consolidation process
309 progresses (that is, decrease of sample porosity), thermal conductivity increases even under the
310 same effective pressure conditions (Figure 7b).
311 In the light of the observation that the thermal conductivity of a sediment core sample is
312 more directly and strongly dependent on porosity than effective pressure conditions, we show the
313 relationship between measured thermal conductivity and porosity estimated from the drained water
314 volume of the six sediment core samples in Figure 8a. A clear trend is observed for all of the
315 samples in which the thermal conductivity increases with decreasing porosity. Although the
316 detailed curves differed between samples owing to differences in lithology and mineral
317 composition, the relationship between thermal conductivity and porosity is essentially the same.

In sedimentary rocks, there is a well-known relationship, called the mixing law, between bulk thermal conductivity in a water saturated state and porosity, as follows:

$$\lambda_{Bulk} = \lambda_{Water}^{\phi} \lambda_{Grain}^{(1-\phi)} \quad (2)$$

or

$$\ln(\lambda_{Bulk}) = \phi \ln(\lambda_{Water}/\lambda_{Grain}) + \ln(\lambda_{Grain}), \quad (3)$$

where λ_{Bulk} is the bulk thermal conductivity of a water-saturated rock, λ_{Water} and λ_{Grain} are the thermal conductivities of pore water and solid grains, respectively, and ϕ is the fractional porosity of the rock sample (e.g., Pribnow and Sass, 1995 and Lin et al., 2011).

We combined all of the data pairs (n = 84) of thermal conductivity and porosity, and then obtained a linear regression following Eq. (3) using least-squares analysis (Figure 8b):

$$\ln(\lambda_{Bulk}) = -1.09\phi + 0.977 \quad (4)$$

or

$$\lambda_{Bulk} = \exp(-1.09\phi + 0.977), \quad (5)$$

where λ_{Bulk} is in $Wm^{-1}K^{-1}$, ϕ is the dimensionless fractional porosity, and $R^2 = 0.84$. From this regression, we calculate the thermal conductivity of solid grains λ_{Grain} and water λ_{Water} by extrapolation; namely, by setting the porosity to 0 and 1, respectively. The results indicate that $\lambda_{Grain} = 2.66$ $Wm^{-1}K^{-1}$ and $\lambda_{Water} = 0.89$ $Wm^{-1}K^{-1}$. The calculated λ_{Grain} is almost the same as 2.6 $Wm^{-1}K^{-1}$, which is the best value assumed for fitting the experimental thermal conductivity values of Tobin et al. (2015b). The calculated λ_{Water}, however, is slightly larger than the typical sea water value (0.61 $Wm^{-1}K^{-1}$ at 25 °C and atmospheric pressure, Jamieson and Tudhope, 1970) probably caused by the extrapolation of the porosity range from an upper limit of 0.6 in our experiments to 1.0 for the state of water alone.

5. Estimation of Thermal Conductivity in the Accretionary Prism at NanTroSEIZE Drilling Site C0002

The pressure and temperature conditions of both sediments and basement likely change during subduction. An increase of pressure is expected to make soft sediments with high porosity and abundant pore water initially compact/consolidate and significantly decrease their porosity during subduction and/or accretion, which may consequently change their physical properties including thermal conductivity. However, this is not readily testable owing to the very limited number of core samples retrieved from deep drilling site C0002. Consequently, only a few data points have been reported deeper than ~1100 mbsf with a maximum depth of 3262.5 mbsf: a few from 2170–2215 mbsf in borehole C0002P and one from 2836.5–2848.5 mbsf in borehole C0002T (Tobin et al., 2015b; Jin et al., 2019). Luckily, porosity was determined by moisture and density (MAD) measurements over almost the whole penetrated depth range using intact handpicked cuttings samples, from which artificial cuttings were excluded, and verified by the limited core samples. A reliable porosity depth profile was thus established (Figure 9a after Tobin et al., 2015b and Kitajima et al., 2017).

Furthermore, a full data set of elastic P-wave velocities in site C0002 from seafloor to 3058.5 mbsf was obtained from drill logs at different depth intervals in boreholes C0002A, C0002F, and C0002P, respectively (Kitajima et al., 2017; Hamada et al., 2018). The log data indicates that P-wave velocity (*Vp*) increases gradually and monotonously with depth to ~2000 mbsf, but remains essentially constant between ~2200 and ~3050 mbsf (Figure 9b). Kitajima et al. (2017) used this *Vp* depth profile to estimate the in-situ porosity depth profile of sediments at site

C0002 to ~3050 mbsf based on the following empirical relationship developed by Erickson and Jarrard (1998).

$$Vp = 1.11 + 0.178\phi + 0.305/[(\phi + 0.135)^2 + 0.0775]$$

$$+ 0.61\ (V_{sh} - 1)\{\tanh[20(\phi - 0.39)] - |\tanh[20(\phi - 0.39)]\ |\}, \qquad (6)$$

where Vp is in km/s, V_{sh} is shale fraction, and fractional porosity ϕ is dimensionless. The data from site C0002 are well fit with $V_{sh} = 0.66$ ($R^2 = 0.74$) and this relation is used to determine the in-situ ϕ from the Vp data, shown as Figure 9c (Kitajima et al., 2017).

As mentioned in section 4, we obtained an empirical relationship (Eq. (5)) between thermal conductivity and porosity from measurements under high confining and pore pressures using sediment core samples collected from the input site that will ultimately subduct and/or accrete to the accretionary prism. The porosity of the sediment core samples ranges from ~60% to ~20%, which nearly matches the porosity of sediments down to ~3000 mbsf at site C0002. The empirical equation can thus be used to estimate the thermal conductivity depth profiles for site C0002 from porosities both measured by MAD (Figure 9a) and derived from Vp (Figure 9c). The results show that the estimated thermal conductivity increases gradually and monotonously with depth, from ~1.3 $Wm^{-1}K^{-1}$ at the seafloor to ~2.2 $Wm^{-1}K^{-1}$ at ~3050 mbsf (Figure 9d).

In principle, porosities of the core and intact handpicked cuttings samples were measured by MAD at atmospheric pressure, and thermal conductivities estimated from the MAD porosities may therefore represent values under ambient pressure conditions rather than high-pressure conditions. However, the porosities derived from the Vp log data are in-situ porosities and the thermal conductivity from the Vp-derived porosity may better represent in-situ thermal properties than that of core samples under atmospheric pressure conditions. The thermal conductivities estimated from the Vp-derived porosities are larger than those from the MAD porosities between

~500 and 2000 mbsf by approximately 5%–10%. Hoffman and Tobin (2004) also reported the *Vp*-derived porosities are larger than the MAD porosity in the Nankai Trough accretionary prism off of Muroto. However, similar thermal conductivities are estimated above ~500 mbsf and deeper than ~2000 mbsf. The pressure at depths above ~500 mbsf is relatively smaller and its effects are not particularly strong; however, below ~2000 mbsf, the sediments harden and rebound owing to stress relief and its effects are not significant.

The thermal conductivity measured onboard using core samples from 2170–2215 mbsf have a mean and standard deviation of 1.73±0.08 $Wm^{-1}K^{-1}$ (calculated based on all of the individual values in Table T36 of Tobin et al., 2015b), which is within the estimated thermal conductivity range by the MAD porosities in this study but close to the lower boundary. In addition, the wide porosity distribution (~20%–40%) at 2170–2215 mbsf suggests a significant scattering of physical properties over this depth interval (Figure 9a). The scatter is caused by including porosity data from the fault zone samples. At a depth of ~2840 mbsf, the measured thermal conductivity of a core sample was reported to be ~2.2 $Wm^{-1}K^{-1}$ (Jin et al., 2019) and showed a similar or slightly larger value than our estimates over the same depth range.

At site C0002, the in-situ temperature has been estimated to increase with depth and reach ~100 °C at ~3000 mbsf (Sugihara et al., 2014; Yabe et al., 2019). Indeed, temperature effects on the thermal conductivity of the Nankai sediments should also be examined for estimating in-situ thermal conductivity. Lin et al. (2018) reported that thermal conductivity changed less than ~7% over a temperature range between room temperature and 100 °C for a basalt core sample taken from the same site C0012, which suggests that temperature should have a smaller effect on thermal conductivity than pressure. In light of the absence of data regarding the temperature effect of thermal conductivity for oceanic sediments, we do not presently consider the effects of temperature

409 on the in-situ thermal conductivity. Nevertheless, we are designing further improvements to our
410 current thermal property measurement system to allow measurements under simultaneously high
411 temperature and high pressure conditions to address these effects on the thermal conductivity of
412 accretionary prism sediments.
413
414 **6. Conclusions**
415
416 Knowledge of sediment thermal conductivity is necessary for understanding the thermal
417 structure of active seismogenic zones, such as the Nankai Trough subduction zone, SW Japan. If
418 available, thermal conductivities may be easily determined by laboratory measurements using drill
419 core samples. However, only a very limited number of drill core samples have been collected in
420 the Nankai Trough accretionary prism by the Nankai Trough Seismogenic Zone Experiment
421 (NanTroSEIZE), International Oceanic Discovery Program (IODP). Thus, a complete thermal
422 conductivity depth profile in the accretionary prism is not available. The thermal conductivity of
423 water-saturated sediments may depend mainly on their solid grain components and porosity. Based
424 on this consideration, we conducted experiments to determine a quantitative relationship between
425 the thermal conductivity and porosity of the core samples. We used core samples with the same or
426 similar solid grain components as those from the Nankai Trough accretionary prism. Because
427 sediments from sedimentary formations overlaying the in-coming subducting oceanic basement
428 will ultimately subduct in the accretionary wedge, they are expected to have the same or similar
429 solid grain components. We therefore collected whole-round sediment core samples obtained from
430 sedimentary formations at the NanTroSEIZE input site C0012 and measured their thermal

conductivity over a range of effective confining pressures to simulate subduction by changing the sample porosity.

We measured the thermal conductivity of six core samples from a depth range of ~144 to ~518 mbsf at site C0012 under high-pressure conditions to a maximum effective pressure of ~50 MPa corresponding to a depth of more than ~4 kmbsf. We obtain an empirical equation between thermal conductivity λ_{Bulk} in $Wm^{-1}K^{-1}$ and fractional porosity ϕ for the Nankai Trough accretionary prism as $\lambda_{Bulk} = \exp(-1.09\phi + 0.977)$. Based on porosity data sets from the NanTroSEIZE centerpiece site C0002 measured both using core/cuttings samples and derived from P-wave velocity logs, we estimated complete thermal conductivity profiles down to ~3 kmbsf in the Nankai Trough accretionary prism. In principle, the thermal conductivity estimated from porosities measured using the core/cuttings samples may better represent values under atmospheric pressure conditions and not in-situ high-pressure conditions. Porosities derived from the P-wave velocity log may better represent the in-situ porosities. Nevertheless, the two thermal conductivity profiles show a consistent trend with no significant differences. The profiles also agree with existing thermal conductivity data measured using limited core samples from the accretionary prism.

Acknowledgments

This study used sediment core samples retrieved from NanTroSEIZE expeditions 322 and 333 provided by the IODP. Constructive comments from two anonymous reviewers were helpful for improving the manuscript. The authors gratefully acknowledge Osamu Matsubayashi for sharing a core sample (C0012G01R4) and Toshiya Kanamatsu, Saneatsu Saito, Masataka Kinoshita, and

454 the other NanTroSEIZE scientists for their helpful discussions. Part of the work was supported by
455 Grants-in-Aid for Scientific Research 16H04065 and 19H00717 of the Japan Society for the
456 Promotion of Science (JSPS), Japan. We thank Esther Posner from Edanz Group for editing a draft
457 of this manuscript. All experimental data will be available on the Pangaea data publisher for earth
458 and environmental science (https://doi.org/10.1594/PANGAEA. 'TBD').
459

460 **References**

461

462 Abdulagatova, Z., Abdulagatov, I. M., and Emirov, V. N., 2009, Effect of temperature and
463 pressure on the thermal conductivity of sandstone. *Int. J. Rock Mech. Min. Sci.*, 46, 1055–
464 1071. https://doi:10.1016/j.ijrmms.2009.04.011
465 Ando, M., 1975, Source mechanisms and tectonic significance of historical earthquakes along
466 the Nankai Trough, Japan. *Tectonophysics*, 27, 119–140.
467 Byrne, T. B., Lin, W., Tsutsumi, A., Yamamoto, Y., Lewis, J. C., Kanagawa, K., . . . Kimura, G.
468 (2009). Anelastic strain recovery reveals extension across SW Japan subduction zone.
469 *Geophysical Research Letters*, 36, L23310. https://doi.org/10.1029/2009GL040749
470 Erickson, S. N., and Jarrard, R. D. (1998). Velocity-porosity relationships for water-saturated
471 siliciclastic sediments. *Journal of Geophysical Research*, *103* (B12), 30,385–30,406.
472 https://doi.org/10.1029/98JB02128
473 Expedition 322 Scientists (2010). Site C0012. In Saito, S., Underwood, M.B., Kubo, Y., and the
474 Expedition 322 Scientists, Proc. IODP 322: Tokyo (Integrated Ocean Drilling Program
475 Management International, Inc.). https://doi:10.2204/iodp.proc.322.104.2010

476 Expedition 333 Scientists (2012a). Expedition 333 summary. In Henry, P., Kanamatsu, T., Moe,
477 K., and the Expedition 333 Scientists, Proc. IODP 333: Tokyo (Integrated Ocean Drilling
478 Program Management International, Inc.). https://doi:10.2204/iodp.proc.333.101.2012
479 Expedition 333 Scientists (2012b). Site C0012. In Henry, P., Kanamatsu, T., Moe, K., and the
480 Expedition 333 Scientists, Proc. IODP 333: Tokyo (Integrated Ocean Drilling Program
481 Management International, Inc.). https://doi:10.2204/iodp.proc.333.105.2012
482 Franklin, J. A., (Coordinator) (1979). Suggest methods for determining water content, porosity,
483 density, absorption and related properties and swelling and slake-durability index properties,
484 *Int. J. Rock Mech. Min. Sci. & Geomech. Abstr.*, *16*, 141-156.
485 Fulton, P.M., Brodsky, E. E., Kano, Y., Mori, J., Chester, F., Ishikawa, T., Harris, R.N., Lin, W.,
486 Eguchi, N., Toczko, S., Expedition 343, 343T, and KR13-08 Scientists (2013). Low
487 Coseismic Friction on the Tohoku-Oki Fault Determined from Temperature Measurements.
488 *Science*, *342*, 1214-1217, https://doi:10.1126/science.1243641
489 Galson, D. P., Wilson, N. P., Schari, U., and Rybach, L. (1987). A comparison of divided-bar
490 and QTM methods of measuring thermal conductivity. *Geothermics*, *16*, 215–226.
491 Hamada, Y., Kitamura, M., Yamada, Y., Sanada, Y., Sugihara, T., Saito, S., Moe, K., Hirose, T.
492 (2018). Continuous depth profile of the rock strength in the Nankai accretionary prism based
493 on drilling performance parameters. *Scientific Reports*, *8*, 2622. https://doi:10.1038/s41598-
494 018-20870-8
495 Harris, R. N., Schmidt‐Schierhorn, F., and Spinelli, G. (2011). Heat flow along the
496 NanTroSEIZE transect: Results from IODP Expeditions 315 and 316 offshore the Kii
497 Peninsula, Japan, *Geochem. Geophys. Geosyst.*, *12*, Q0AD16,
498 https://doi:10.1029/2011GC003593

499 Harris, R. N., and Wang, K. (2002). Thermal models of the Middle America Trench at the
500 Nicoya Peninsula, Costa Rica, *Geophys. Res. Lett.*, *29*, no.2010.
501 https://doi:10.1029/2002GL015406
502 Heki, K., and Miyazaki, S. (2001). Plate convergence and long-term crustal deformation in
503 Central Japan. *Geophys. Res. Lett.*, *28*, 2313–2316.
504 Hoffman, N.W., and Tobin, H.J. (2004). An empirical relationship between velocity and porosity
505 for underthrust sediments in the Nankai Trough accretionary prism. In: Mikada, H., Moore,
506 G.F., Taira, A., Becker, K., Moore, J.C., Klaus, A. (Eds.), *Proc. ODP, Sci. Results*, 190/196,
507 1-23.
508 Horai, K., and Susaki, J. (1989). The effect of pressure on the thermal conductivity of silicate
509 rocks up to 12 kbar. *Phy. Earth Planetary Interiors*, *55*, 292-305.
510 Jamieson, D.T., and Tudhope, J.S. (1970). Physical property of sea water solutions: thermal
511 conductivity, *Desalination*, *8*, 393-401.
512 Jin, Z., Bedford, J. D., Kitamura, M., Sone, H., Stanislowski, K., Hamada, Y., Kopf, A., Zhang,
513 J., Kitajima, H., Saffer, D. M., Hirose, T., Ikari, M., Kanagawa, K., Kimura, G., Kinoshita,
514 M., Tobin, H. J., Yamaguchi, A., Eguchi, N., Kubo, Y., Maeda, L., Toczko, S. and IODP
515 Expedition 358 Shipboard Scientific Party (2019). Physical properties of the Nankai Trough
516 at Sites C0002, C0024 and C0025, IODP Expedition 358, Paper T51G-0365 presented at
517 2019 Fall Meeting, American Geophysical Union, San Francisco, CA.
518 Kanamori, H. (1972). Tectonic implications of the 1944 Tonankai and the 1946 Nankaido
519 earthquakes. *Phys. Earth Planet. Inter.*, *5*, 129–139.
520 Kinoshita, M., Moore, G., von Huene, R., Tobin, H., and Ranero, C. (2006). The seismogenic
521 zone experiment, *Oceangraph*, *19*, 28-38.

522 Kitajima, H., Saffer, D., Sone, H., Tobin, H., & Hirose, T. (2017). In situ stress and pore pressure
523 in the deep interior of the Nankai accretionary prism, integrated Ocean Drilling Program
524 Site C0002. *Geophysical Research Letters*, *44*, 9644–9652.
525 https://doi.org/10.1002/2017GL075127
526 Kukkonen, I. T., Jokinen, J., and Seipold, U., (1999). Temperature and pressure dependencies of
527 thermal transport properties of rocks: Implications for uncertainties in thermal lithosphere
528 models and new laboratory measurements of high-grade rocks in the central Fennoscandian
529 shield, *Surveys in Geophysics*, *20*, 33–59.
530 Lin, W., Byrne, T., Kinoshita, M., McNeill, L., Chang, C., Lewis, J., Yamamoto, Y., Saffer, D.,
531 Moore, J.C., Wu, H.-Y., Tsuji, T., Yamada, Y., Conin, M., Saito, S., Ito, T., Tobin, H.,
532 Kimura, G., Kanagawa, K., Ashi, J., Underwood, M., Kanamatsu, T. (2016). Distribution of
533 stress state in the Nankai subduction zone, southwest Japan and a comparison with Japan
534 Trench. *Tectonophysics*, *692*, 120-130. https://doi:10.1016/j.tecto.2015.05.008
535 Lin, W., Fulton, P. M., Harris, R. N., Tadai, O., Matsubayashi, O., Tanikawa, W., and Kinoshita,
536 M. (2014). Thermal conductivities, thermal diffusivities, and volumetric heat capacities of
537 core samples obtained from the Japan Trench Fast Drilling Project (JFAST). *Earth, Planets*
538 *and Space*, *66*, no.48. https://doi:10.1186/1880-5981-66-48
539 Lin, W., Tadai, O., Hirose, T., Tanikawa, W., Takahashi, M., Mukoyoshi, H., Kinoshita, M.,
540 (2011). Thermal conductivities under high pressure in core samples from IODP
541 NanTroSEIZE drilling site C0001. *Geochem. Geophys. Geosyst.*, *12*, no.Q0AD14,
542 https://doi:10.1029/2010GC003449
543 Lin, W., Tadai, O., Kinoshita, M., Kameda, J., Tanikawa, W., Hirose, T., Hamada, Y., and
544 Matsubayashi, O. (2018). Thermal conductivity changes in subducting basalt, Nankai

545 subduction zone, SW Japan: An estimation from laboratory measurements under separate
546 high-pressure and high-temperature conditions, in Byrne, T. et al., eds., Geology and
547 Tectonics of Subduction Zones: A Tribute to Gaku Kimura: *Geological Society of America*
548 *Special Paper 534*, 35–50, https://doi.org/10.1130/2018.2534(02).
549 Miyazaki, S., and Heki, K. (2001). Crustal velocity field of southwest Japan: subduction and arc-
550 arc collision. *J. Geophys. Res.*, *106* (B3), 4305–4326. http://doi.org/10.1029/2000JB900312
551 Mizutani, T., Hirauchi, K-I., Lin, W., and Sawai, M., (2017), Depth dependence of the frictional
552 behavior of montmorillonite fault gouge: Implications for seismicity along a décollement
553 zone, *Geophys. Res. Lett.*, *44*, 5383–5390. http://doi:10.1002/2017GL073465
554 Morin, R., and Silva, A.J. (1984). The effects of high pressure and high temperature on some
555 physical properties of ocean sediments. *J. Geophysical Res.*, *89*, 511-526.
556 Mottaghy, D., Vosteen, H.D., and Schellschmidt, R. (2008). Temperature dependence of the
557 relationship of thermal diffusivity versus thermal conductivity for crystalline rocks. *Int.*
558 *Journal of Earth Sciences*, *97*, 435-442. http://doi: 10.1007/s00531-007-0238-3
559 Oohashi, K., Lin, W., Wu, H.-Y., Yamaguchi, A., & Yamamoto, Y. (2017). Stress state in the
560 Kumano Basin and in slope sediment determined from anelastic strain recovery: Results
561 from IODP Expedition 338 to the Nankai Trough. *Geochemistry, Geophysics, Geosystems*,
562 *18*, 3608–3616. https://doi.org/10.1002/2017GC007137
563 Osako, K., Ito, E., and Yoneda, A. (2004). Simultaneous measurements of thermal conductivity
564 and thermal diffusivity for garnet and olivine under high pressure. *Phy. Earth Planetary*
565 *Interiors*, *143-144*, 311-320. http://doi:10.1016/j.pepi.2003.10.010

566 Park, J.-O., Tsuru, T., Kodaira, S., Cummins, P.R., and Kaneda, Y. (2002). Splay fault branching
567 along the Nankai subduction zone. *Science*, *297*, 1,157–1,160.
568 https://doi.org/10.1126/science.1074111
569 Pribnow, D., and Sass, J.H. (1995). Determination of thermal conductivity from deep boreholes,
570 *J. Geophys. Res.*, *100*, 9981-9994.
571 Pribnow, D., Williams, C.F., Sass, J.H., and Keating, R. (1996). Thermal conductivity of water-
572 saturated rocks from the KTB pilot hole at temperature of 25 to 300 °C, *Geophys. Res. Lett.*,
573 *23*, 391-394.
574 Saito, S., Underwood, M.B., and Kubo, Y. (2009). NanTroSEIZE Stage 2: subduction inputs.
575 IODP Sci. Prosp. 322. http://dx.doi.org/10.2204/iodp.sp.322.2009.
576 Sass, J. H., Stone, C., and Munroe, R.J. (1984). Thermal conductivity determinations on solid
577 rock — a comparison between a steady-state divided bar apparatus and a commercial
578 transient line-source device. *Jour. Volcanol. Geotherm. Res.*, *20*, 145-153.
579 Scholz, C. H. (1998). Earthquakes and friction laws, *Nature*, 391, 37-42.
580 https://doi.org/10.1038/34097
581 Seno, T., Stein, S., Gripp, A.E. (1993). A model for the motion of the Philippine Sea Plate
582 consistent with NUVEL-1 and geological data. *Journal of Geophysical Research*, *98*,
583 17941–17948.
584 Seipold, U., 1998, Temperature dependence of thermal transport properties of crystalline rocks -a
585 general low, Tectonophysics, v.291, p.161-171.
586 Seipold, U., and Huenges, E. (1998). Thermal properties of gneisses and amphibolites high
587 pressure and high temperature investigations of KTB-rock samples, *Tectonophysics*, *291*,
588 173-178.

589 Spinelli, G.A. (2014). Long-distance fluid and heat transport in the oceanic crust entering the
590 Nankai subduction zone, NanTroSEIZE transect. *Earth and Planetary Science Letters*, *389*,
591 86-94.
592 Stesky, R.M., Brace, W.F., Riley, D.K., Robin, P.-Y. F. (1974). Friction in faulted rock at high
593 temperature and pressure, *Tectonophysics*, *23*, 177-203. https://doi.org/10.1016/0040-
594 1951(74)90119-X
595 Sugihara, T., Kinoshita, M., Araki, E., Kimura, T., Kyo, M., Namba, Y., Kido, Y., Sanada, Y.,
596 Moe, K. (2014). Re-evaluation of temperature at the updip limit of locked portion of Nankai
597 megasplay inferred from IODP Site C0002 temperature observatory, *Earth, Planets and*
598 *Space*, *66*, no.107, https://doi:10.1186/1880-5981-66-107
599 Tanikawa, W., Hirose, T., Mukoyoshi, H., Tadai, O., and Lin, W. (2013). Fluid transport
600 properties in sediments and their role in large slip near the surface of the plate boundary
601 fault in the Japan Trench, *Earth and Planetary Science Letters*, *382*, 150–160.
602 https://doi.org/10.1016/j.epsl.2013.08.052
603 Tanikawa, W., Tadai, O., Morita, S., Lin, W., Yamada, Y., Sanada, Y., Moe, K., Kubo, Y.,
604 Inagaki, F. (2016). Thermal properties and thermal structure in the deep-water coalbed basin
605 off the Shimokita Peninsula, Japan, *Marine and Petroleum Geology*, *73*, 445-461.
606 Tobin, H., Hirose, T., Saffer, D., Toczko, S., Maeda, L., Kubo, Y., Boston, B., Broderick, A.,
607 Brown, K., Crespo-Blanc, A., Even, E., Fuchida, S., Fukuchi, R., Hammerschmidt, S.,
608 Henry, P., Josh, M., Jurado, M.J., Kitajima, H., Kitamura, M., Maia, A., Otsubo, M.,
609 Sample, J., Schleicher, A., Sone, H., Song, C., Valdez, R., Yamamoto, Y., Yang, K.,
610 Sanada, Y., Kido, Y., and Hamada, Y. (2015a). Expedition 348 summary. In Tobin, H.,
611 Hirose, T., Saffer, D., Toczko, S., Maeda, L., Kubo, Y., and the Expedition 348 Scientists,

612 Proc. IODP, 348: College Station, TX (Integrated Ocean Drilling Program).
613 https://doi.org/10.2204/iodp.proc.348.101.2015
614 Tobin, H., Hirose, T., Saffer, D., Toczko, S., Maeda, L., Kubo, Y., Boston, B., Broderick, A.,
615 Brown, K., Crespo-Blanc, A., Even, E., Fuchida, S., Fukuchi, R., Hammerschmidt, S.,
616 Henry, P., Josh, M., Jurado, M.J., Kitajima, H., Kitamura, M., Maia, A., Otsubo, M.,
617 Sample, J., Schleicher, A., Sone, H., Song, C., Valdez, R., Yamamoto, Y., Yang, K.,
618 Sanada, Y., Kido, Y., and Hamada, Y. (2015b), Site C0002. In Tobin, H., Hirose, T., Saffer,
619 D., Toczko, S., Maeda, L., Kubo, Y., and the Expedition 348 Scientists, Proc. IODP, 348:
620 College Station, TX (Integrated Ocean Drilling Program).
621 https://doi.org/10.2204/iodp.proc.348.103.2015
622 Tobin, H., Hirose, T., Ikari, M., Kanagawa, K., Kimura, G., Kinoshita, M., Kitajima, H., Saffer,
623 D., Yamaguchi, A. Eguchi, N., Maeda, L., Toczko, S., and the Expedition 358 Scientists,
624 (2019a). Expedition 358 Preliminary Report: NanTroSEIZE Plate Boundary Deep Riser 4:
625 Nankai Seismogenic/Slow Slip Megathrust. International Ocean Discovery Program.
626 https://doi.org/10.14379/iodp.pr.358.2019
627 Tobin, H.J., Kimura, G. and Kodaira, S. (2019b). Processes governing giant subduction
628 earthquakes: IODP drilling to sample and instrument subduction zone megathrusts,
629 *Oceanography*, *32*, No.1, Special Issue on Scientific Ocean Drilling: Looking to the Future,
630 80-93.
631 Tobin, H.J., and Kinoshita, M. (2006). Investigations of seismogenesis at the Nankai Trough,
632 Japan. IODP Sci. Prosp. NanTroSEIZE Stage 1. doi:10.2204/iodp.sp.nantroseize1.2006
633 Underwood, M.B., Saito, S., Kubo, Y., and the Expedition 322 Scientists (2010). Expedition 322
634 summary. In Saito, S., Underwood, M.B., Kubo, Y., and the Expedition 322 Scientists, Proc.

635 IODP, 322: Tokyo (Integrated Ocean Drilling Program Management International, Inc.).
636 https://doi.org/10.2204/iodp.proc.322.101.2010
637 Wang, K., Hyndman, R.D., and Yamano, M. (1995). Thermal regime of the Southwest Japan
638 subduction zone: effects of age history of the subducting plate, *Tectonophysics*, 248, 53-69.
639 Xu, Y., Shankland, T.J., Linhardt, S., Rubie, D.C., Langenhorst, F., and Klasinski, K. (2004).
640 Thermal diffusivity and conductivity of olivine, wadsleyyite and ringwoodite to 20 GPa and
641 1373 K. *Phy. Earth Planetary Interiors*, *143-144*, 321-336,
642 https://doi.org/10.1016/j.pepi.2004.03.005.
643 Yabe, S., Fukuchi, R., Hamada, Y., and Kimura, G. (2019). Simultaneous estimation of in situ
644 porosity and thermal structure from core sample measurements and resistivity log data at
645 Nankai accretionary prism. *Earth, Planets and Space*, *71*, no.116.
646 https://doi.org/10.1186/s40623-019-1097-4
647 Yamamoto, Yuzuru, Lin, W., Oda, H., Byrne, T., Yamamoto, Yuhji (2013). Stress states at the
648 subduction input site, Nankai Subduction Zone, using anelastic strain recovery (ASR) data
649 in the basement basalt and overlying sediments. *Tectonophysics*, *600*, 91-98.
650 https://doi.org/10.1016/j.tecto.2013.01.028.
651 Yamano, M., Kinoshita, M., Goto, S., and Matsubayashi, O. (2003). Extremely high heat flow
652 anomaly in the middle part of the Nankai Trough. *Phys. Chem. Earth*, *28*, 487-497.
653
654
655

Table 1. Sample ID, depth, lithological unit, lithology, geological age, and basic physical properties. Density and porosity under atmospheric pressure were determined by the buoyancy method (Franklin, 1979). Lithology and age data are after Expedition 322 Scientists (2010) and Expedition 333 Scientists (2012b). The physical properties of C0012G07RCC are after Lin et al. (2018).

Sample ID*	Depth (mbsf)	Lithological Unit, Lithology and Age	Wet bulk density g/cm^3	Grain density g/cm^3	Porosity %	Thermal conductivity** Wm^{-1}K^{-1}
C0012D05H3	~144	Unit IC, Hemipelagic mud, late Miocene	1.71	2.79	60.6	1.34±0.02
C0012A19R1	~217	Unit II, Siltstone, middle Miocene	1.84	2.79	53.4	1.48±0.01
C0012A23R6	~259	Unit III, Hemipelagic mudstone, middle Miocene	1.88	2.79	50.9	1.47±0.01
C0012A32R3	~341	Unit IV, Hemipelagic mudstone, middle Miocene	1.94	2.79	47.2	1.52±0.03
C0012A43R2	~445	Unit V, Hemipelagic mudstone, middle Miocene	2.04	2.71	39.5	1.50±0.03
C0012G01R4	~518	Unit VI, Calcareous pelagic claystone, early Miocene	2.23	2.86	33.8	1.80±0.07
C0012G07RCC	~573	Unit VII, Basalt, early Miocene	2.57	2.81	3.9 - 8.7***	1.70±0.01

* The core sample name C0012A19R1 denotes that it was retrieved from the site C0012, borehole A, 19th rotary-drilled core, 1st core section. In addition, "H" of C0012D05H3 means hydraulic piston coring system (HPCS), and "CC" of C0012G07RCC is from the core catcher.

** Thermal conductivity was measured in this study under atmospheric pressure and room temperature conditions.

*** The corrected measured porosity was estimated as in the range by Lin et al. (2018).

Figure captions

Figure 1. Topographic map of the NanTroSEIZE study area (modified from Lin et al., 2016). Two red stars show the epicenters of the 1944 Tonankai and 1946 Nankai earthquakes. The circles and labels (e.g., C0012) show the locations of NanTroSEIZE drilling sites. PSP denotes the Philippine Sea Plate and the yellow arrows show the far-field convergence vectors between the Philippine Sea plate and Japan (Heki and Miyazaki, 2001; Miyazaki and Heki, 2001). The red rectangle in the inset shows the location of the main map.

Figure 2. Seismic reflection depth section with tectonic interpretation of the NanTroSEIZE transect, originally published by Park et al. (2002) as section Line 5 (modified from Tobin et al., 2015a). Depths denote the depth below sea level. PSP denotes the Philippine Sea plate. The sediment core samples used in this study were retrieved from input site C0012.

Figure 3. Schematic diagram of the apparatus used in this study (modified from Lin et al., 2018) for thermal conductivity measurements under high confining pressure and high pore pressure conditions. The system comprises a hydrostatic pressure vessel with two servo-controlled syringe pumps, a wire-type line-source sensor in the pressure vessel, a thermal-conductivity meter (QTM-500) to measure thermal conductivity from the wire sensor, and a data logger. One syringe pump provides high pressures up to ~138 MPa for confining pressure, and the other up to ~52 MPa for pore pressure. The pore pressure pump monitors the drained water volume to calculate the change in total pore volume of the water-saturated rock samples associated with sample deformation.

Figure 4. Photos of the sample assembly for thermal conductivity measurements under high confining and pore fluid pressures. (a) Assembly of a half-cylindrical rock sample and a Teflon piece of the same shape and size. (b) Top view of the rock sample and Teflon. (C) Prior to set up.

Figure 5. Examples of thermal conductivity measurements for sediment core sample C0012G0104 at four different confining pressures. The gradient of each data set in semi-logarithmic scale is inversely proportional to thermal conductivity. Labels beside the data plots indicate the effective pressure ($P_{eff} = P_c - P_p$).

Figure 6. The data set of thermal conductivity measurements for sediment core sample C0012A19R1: (a) real data of confining and pore pressures and measurement points of thermal conductivity; (b) estimated porosity; and (c) thermal conductivity results. The porosity under high pressure was estimated from the porosity under atmospheric pressure (initial porosity) and pore volume change detected by the pore water drainage. We increased the confining pressure stepwise to simulate subsidence and compaction and held the pore pressure constant at 10 MPa except for the first and last steps of the test. While keeping the pressure constant, the pore water drainage progressed but its rate gradually decreased. The symbol "+" in (a) indicates the time points at which thermal conductivity measurements were collected. This test lasted ~43 days with accurate pressure control by the pumps over this duration.

716 Figure 7. Relationships between measured thermal conductivity and effective pressure of the six
717 sediment core samples alongside a basalt sample after Lin et al. (2018). (a) and (b) show the
718 same data but in different effective pressure ranges. We measured the thermal conductivity six
719 or seven times at each point (see "+" in Figure 6a). The data points in these figures represent
720 the mean values of the measured thermal conductivities. The data of C12G07RCC are from Lin
721 et al. (2018).
722
723 Figure 8. Relationships between measured thermal conductivity and estimated porosity of the six
724 sediment core samples: (a) as individual samples and (b) as all of the six samples. The red curve
725 shows a logarithmic regression line based on all of the data. As in Figure 7, each plot shows the
726 mean value of the measured thermal conductivities at the same time point.
727
728 Figure 9. Depth profiles of (a) porosity determined by MAD measurements using core samples
729 and intact handpicked cuttings from site C0002 after Tobin et al. (2015b). (b) P-wave velocity
730 *Vp* obtained from borehole C0002A in green, C0002F in blue, C0002P in black, and a moving
731 average in red after Kitajima et al. (2017). (c) Porosity (%) derived from *Vp* shown in (b) after
732 Kitajima et al. (2017). The colors of the curves mean are the same as (b). (d) Thermal
733 conductivity profiles estimated by Eq. (5) using the porosity by MAD measurements (small
734 circles) and porosity derived by the moving average of *Vp* (red curve).
735
736
737

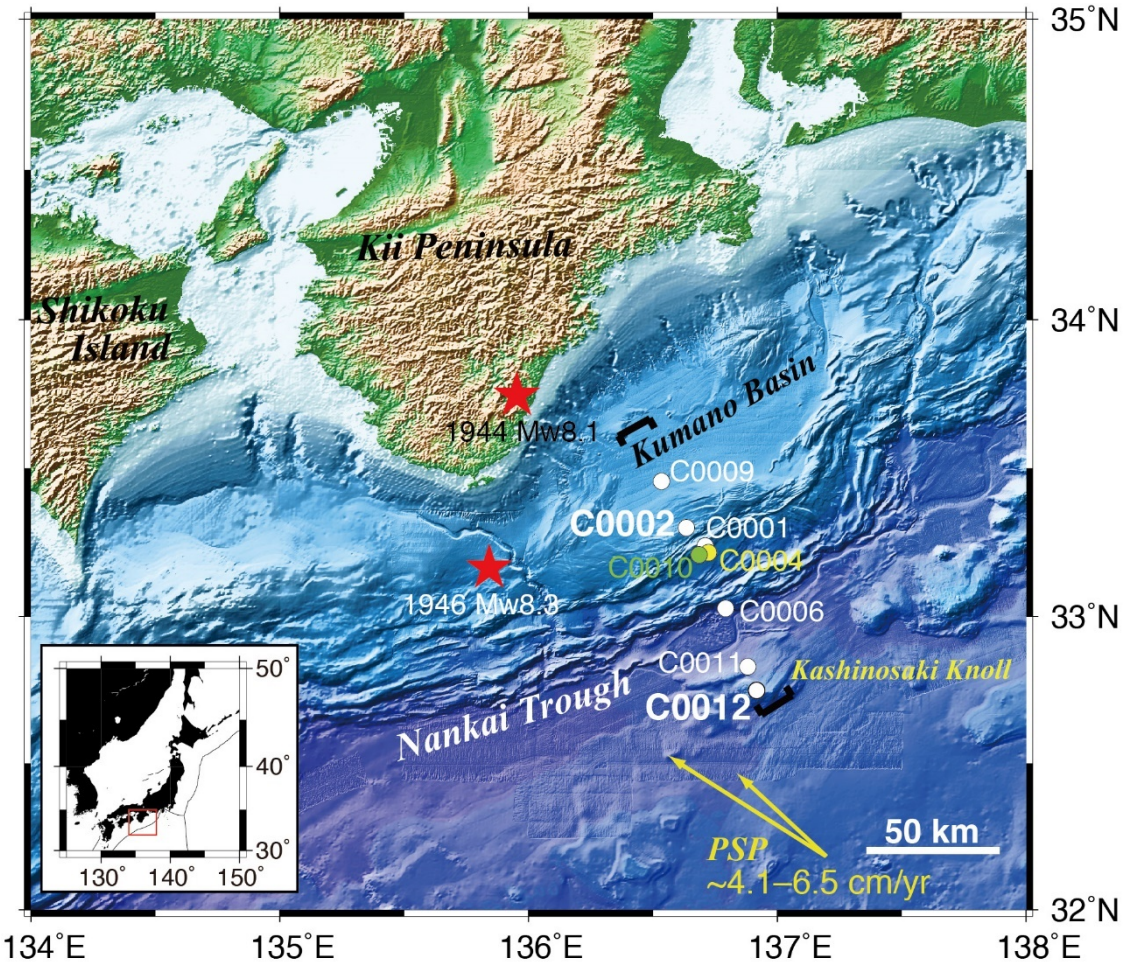

Figure 1. Topographic map of the NanTroSEIZE study area (modified from Lin et al., 2016). Two red stars show the epicenters of the 1944 Tonankai and 1946 Nankai earthquakes. The circles and labels (e.g., C0012) show the locations of NanTroSEIZE drilling sites. PSP denotes the Philippine Sea Plate and the yellow arrows show the far-field convergence vectors between the Philippine Sea plate and Japan (Heki and Miyazaki, 2001; Miyazaki and Heki, 2001). The red rectangle in the inset shows the location of the main map.

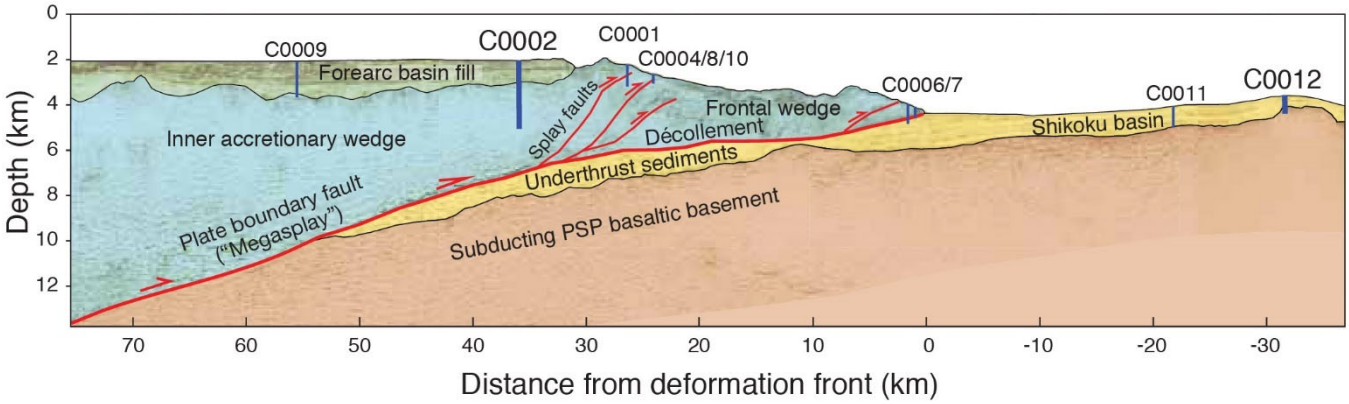

Figure 2. Seismic reflection depth section with tectonic interpretation of the NanTroSEIZE transect, originally published by Park et al. (2002) as section Line 5 (modified from Tobin et al., 2015a). Depths denote the depth below sea level. PSP denotes the Philippine Sea plate. The sediment core samples used in this study were retrieved from input site C0012.

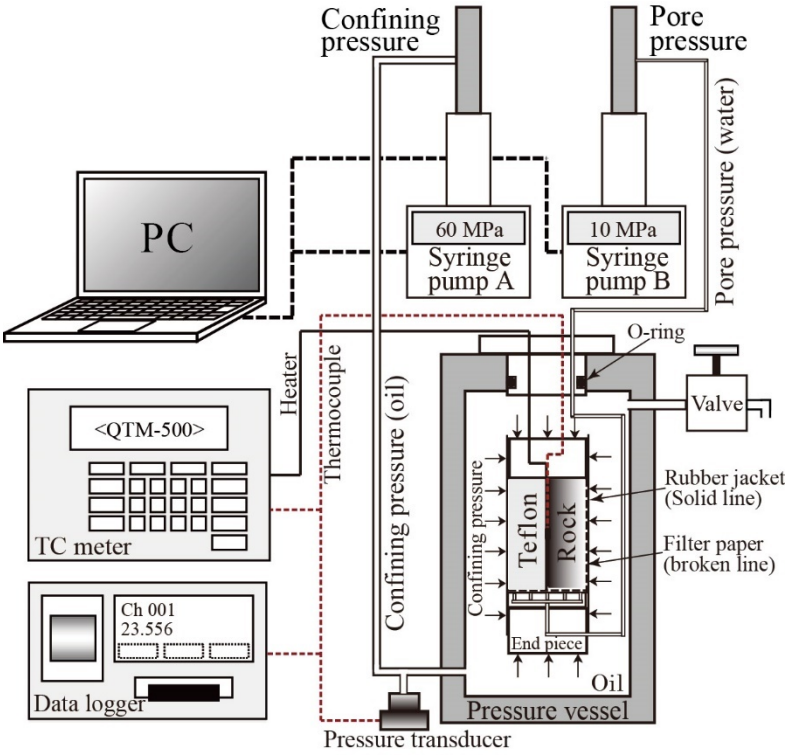

Figure 3. Schematic diagram of the apparatus used in this study (modified from Lin et al., 2018) for thermal conductivity measurements under high confining pressure and high pore pressure conditions. The system comprises a hydrostatic pressure vessel with two servo-controlled syringe pumps, a wire-type line-source sensor in the pressure vessel, a thermal-conductivity meter (QTM-500) to measure thermal conductivity from the wire sensor, and a data logger. One syringe pump provides high pressures up to ~138 MPa for confining pressure, and the other up to ~52 MPa for pore pressure. The pore pressure pump monitors the drained water volume to calculate the change in total pore volume of the water-saturated rock samples associated with sample deformation.

Figure 4. Photos of the sample assembly for thermal conductivity measurements under high confining and pore fluid pressures. (a) Assembly of a half-cylindrical rock sample and a Teflon piece of the same shape and size. (b) Top view of the rock sample and Teflon. (C) Prior to set up.

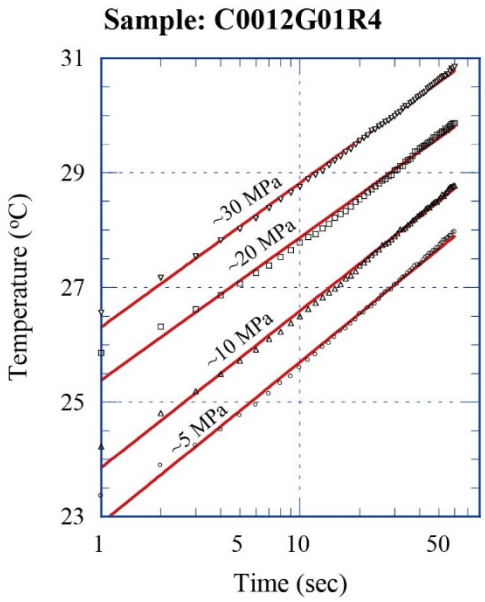

Figure 5. Examples of thermal conductivity measurements for sediment core sample C0012G0104 at four different confining pressures. The gradient of each data set in semi-logarithmic scale is inversely proportional to thermal conductivity. Labels beside the data plots indicate the effective pressure ($P_{eff} = P_c - P_p$).

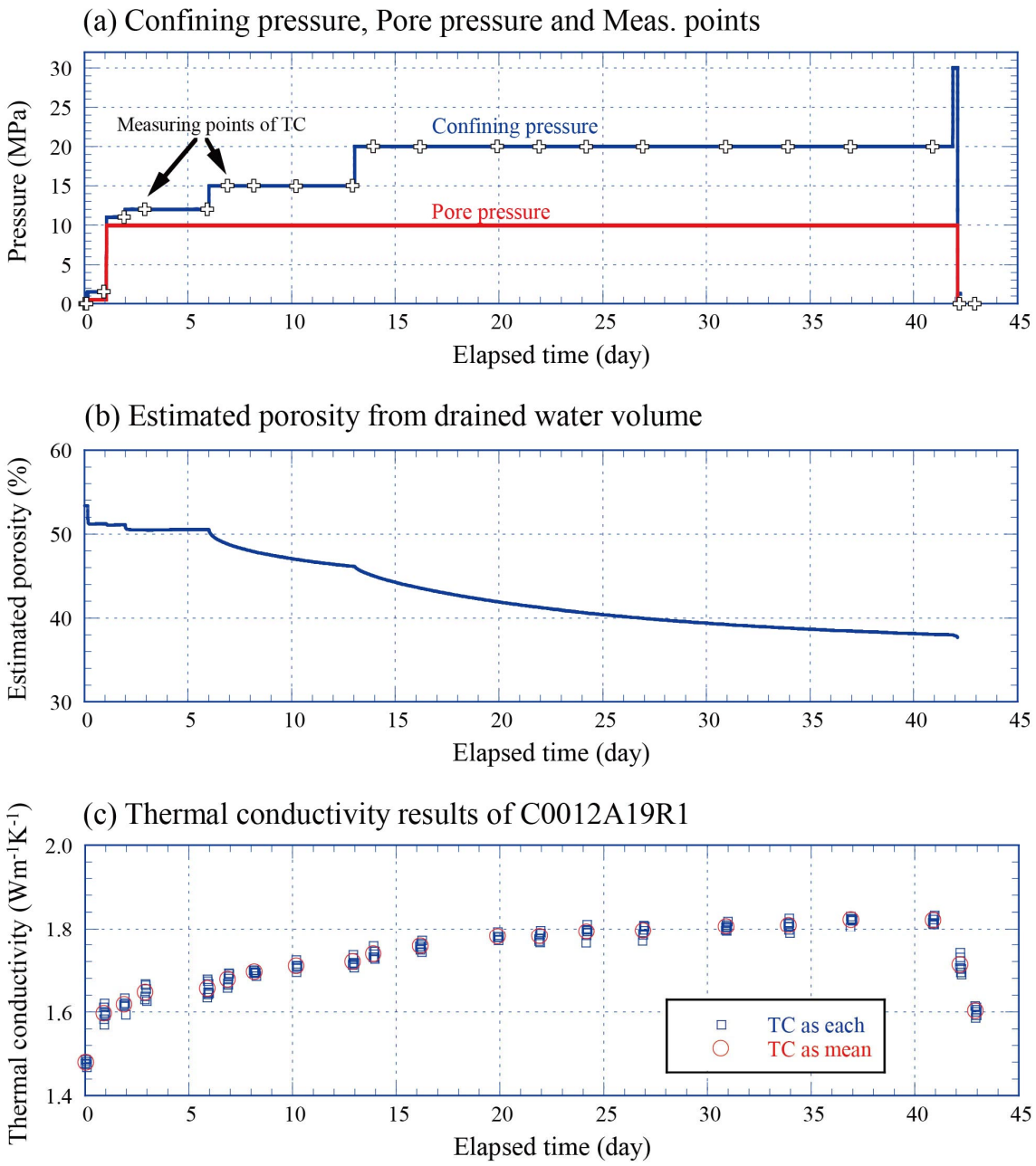

Figure 6. The data set of thermal conductivity measurements for sediment core sample C0012A19R1: (a) real data of confining and pore pressures and measurement points of thermal conductivity; (b) estimated porosity; and (c) thermal conductivity results. The porosity under high pressure was estimated from the porosity under atmospheric pressure (initial porosity) and pore volume change detected by the pore water drainage. We increased the confining pressure stepwise to simulate subsidence and compaction and held the pore pressure constant at 10 MPa except for the first and last steps of the test. While keeping the pressure constant, the pore water drainage progressed but its rate gradually decreased. The symbol "+" in (a) indicates the time points at which thermal conductivity measurements were collected. This test lasted ~43 days with accurate pressure control by the pumps over this duration.

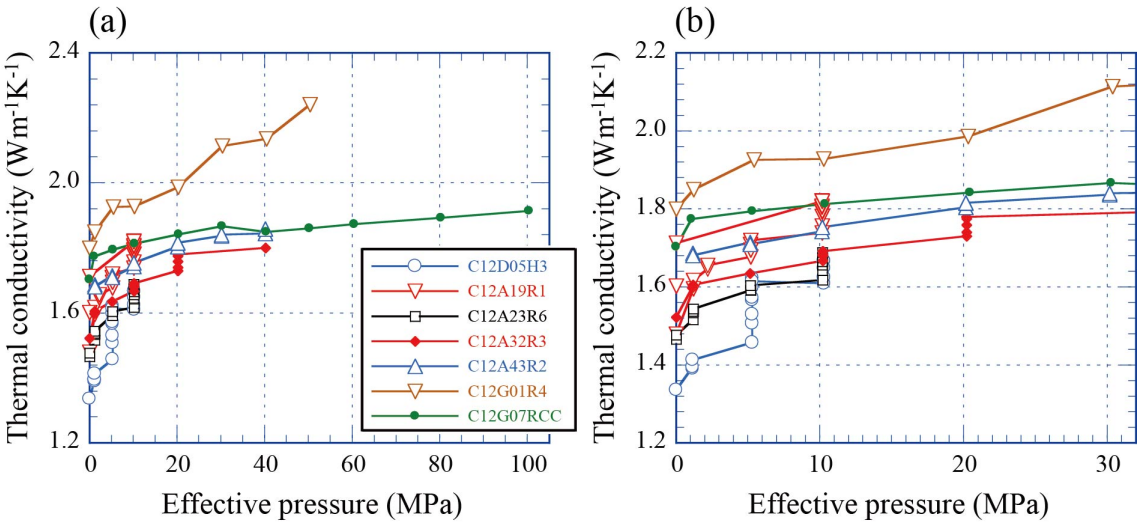

Figure 7. Relationships between measured thermal conductivity and effective pressure of the six sediment core samples alongside a basalt sample after Lin et al. (2018). (a) and (b) show the same data but in different effective pressure ranges. We measured the thermal conductivity six or seven times at each point (see "+" in Figure 6a). The data points in these figures represent the mean values of the measured thermal conductivities. The data of C12G07RCC are from Lin et al. (2018).

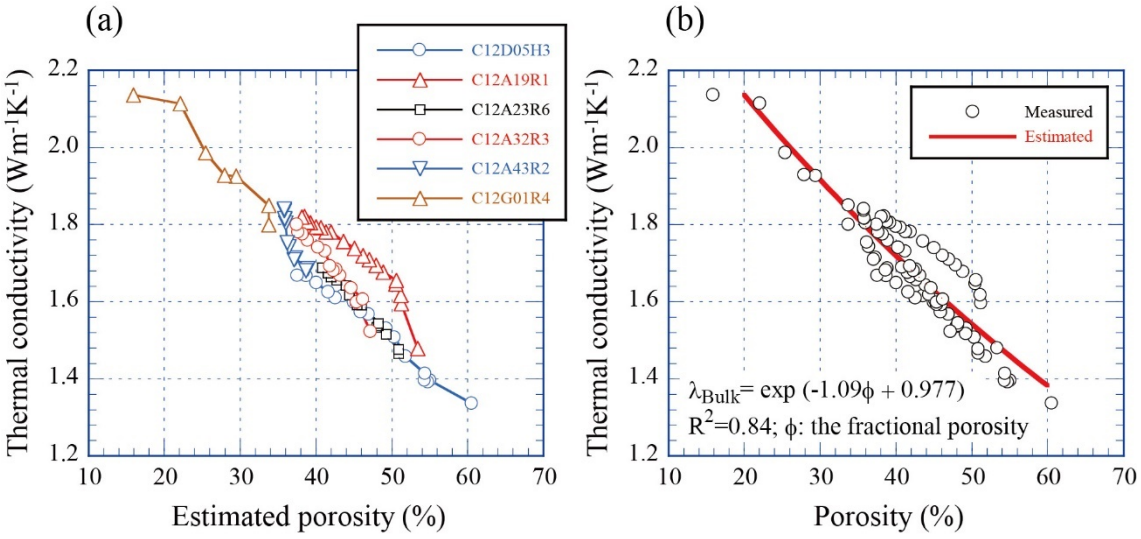

Figure 8. Relationships between measured thermal conductivity and estimated porosity of the six sediment core samples: (a) as individual samples and (b) as all of the six samples. The red curve shows a logarithmic regression line based on all of the data. As in Figure 7, each plot shows the mean value of the measured thermal conductivities at the same time point.

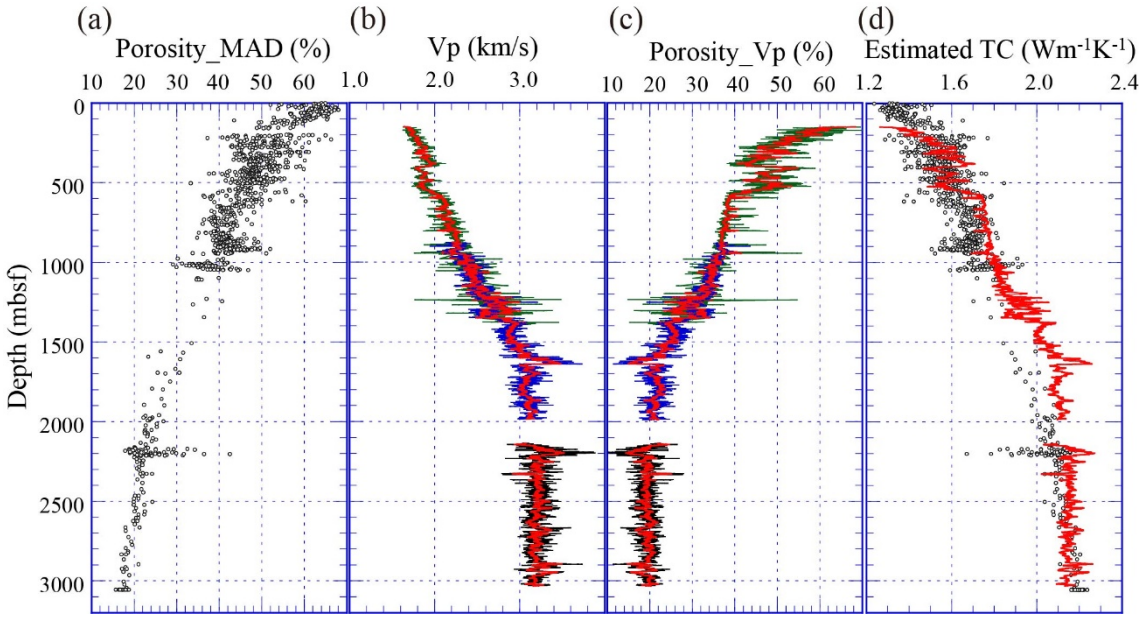

Figure 9. Depth profiles of (a) porosity determined by MAD measurements using core samples and intact handpicked cuttings from site C0002 after Tobin et al. (2015b). (b) P-wave velocity *Vp* obtained from borehole C0002A in green, C0002F in blue, C0002P in black, and a moving average in red after Kitajima et al. (2017). (c) Porosity (%) derived from *Vp* shown in (b) after Kitajima et al. (2017). The colors of the curves mean are the same as (b). (d) Thermal conductivity profiles estimated by Eq. (5) using the porosity by MAD measurements (small circles) and porosity derived by the moving average of *Vp* (red curve).